

Exceptionally high carrier mobility in hexagonal diamond

Zirui He,^{1,2} Shang-Peng Gao,^{1,2,*} and Meng Chen^{2,†}

¹College of Smart Materials and Future Energy, Fudan University, Shanghai 200433, China

²Shanghai Advanced Silicon Technology Co., Ltd., Shanghai 201616, China

Hexagonal diamond (h-diamond), or Lonsdaleite, has been reported to be a wide-bandgap semiconductor with high thermal conductivity and hardness. Our *ab initio* calculations reveal its exceptionally high carrier mobility at room temperature. Along *xy* and *z* directions, the hole mobilities are 5631 and 5552 cm²V⁻¹s⁻¹, and the electron mobilities are 11462 and 28464 cm²V⁻¹s⁻¹, respectively. These values are significantly superior to the mobility of most known semiconductors including cubic diamond. The small effective masses in h-diamond, comparable to those in cubic diamond, cannot explain its substantially higher mobility. Instead, two crucial mechanisms are uncovered: selection rules that considerably suppress hole scattering induced by transverse acoustic phonons, and a spatial decoupling effect where electronic wavefunctions concentrated in lattice interstitials lead to minimal overlap with scattering potentials.

I. INTRODUCTION

Diamond, long prized as a gemstone, is also regarded as the “ultimate” wide-bandgap semiconductor material because of its excellent physical properties [1]. While most semiconductors may show good performance in certain properties, they often face inherent limitations in other critical characteristics. For example, GaAs has high electron mobility yet low hole mobility and thermal conductivity [2]; β -Ga₂O₃ has an ultrawide bandgap and large breakdown field, whereas its carrier mobility and thermal conductivity are unsatisfactory [3]. In contrast, diamond offers a unique combination of a series of key properties, including its high carrier mobility, high thermal conductivity, ultrawide bandgap, and high breakdown field [1]. These intrinsic characteristics position it at the frontier of future electronics operating under the most extreme conditions of high power, frequency, and temperature [4].

In addition to the well-known cubic structure, diamond can also crystallise in the hexagonal phase. Hexagonal diamond (h-diamond), also referred to as Lonsdaleite [5], was both discovered in meteorites [6] and experimentally synthesised [7] in the 1960s. In contrast to cubic diamond (c-diamond) with a stacking sequence of ABCABC... along the (111) directions, it exhibits an ABAB... stacking. Although far less explored than the well-known cubic phase, existing studies have shown that the properties of h-diamond are comparable to, or even superior to, those of c-diamond. For example, Pan *et al.* [8] revealed a 58% higher indentation strength of h-diamond than that of its cubic counterpart. Regarding lattice thermal conductivity, studies on h-diamond report scattered values [9–11], which are approximately 20–30% lower than that of c-diamond, yet still considerably higher than those of most known semiconductors.

In this work, motivated by the recent success in the experimental synthesis of its highly-ordered bulk sam-

ples [12], we thoroughly investigate the carrier mobility of h-diamond using fully *ab initio* calculations, revealing that its mobility significantly exceeds that of most known semiconductor materials. Based on group theory and the spatial distributions of charge density and scattering potential, we further uncover two crucial mechanisms as the physical origins of its high mobility, thereby guiding the discovery and design of novel high-mobility materials.

II. RESULTS

A. Phonon-limited carrier mobility

The calculated carrier mobilities of both phases are shown in Fig. 1. For c-diamond, the room-temperature hole mobility (μ_h) and electron mobility (μ_e) are predicted to be 2543 and 2068 cm²V⁻¹s⁻¹, respectively, in good agreement with experimental values [13]. Regarding h-diamond, its carrier mobilities are found to be much higher. At 300 K, the hole mobilities are $\mu_h^{\perp c} = 5631$ and $\mu_h^{\parallel c} = 5552$ cm²V⁻¹s⁻¹. The electron mobilities are even higher, with $\mu_e^{\perp c} = 11462$ and $\mu_e^{\parallel c} = 28464$ cm²V⁻¹s⁻¹. These values are superior to the typical mobility of most known high-mobility semiconductors, for example, Ge ($\mu_h = 1820$ cm²V⁻¹s⁻¹ [14]) for holes and GaAs ($\mu_e = 8900$ cm²V⁻¹s⁻¹ [15]) for electrons, also overcoming the limitation of most conventional semiconductors where only one carrier type exhibits high mobility. While the predicted hole mobility agrees well with the result in Ref. 16, our calculated electron mobility significantly exceeds the reported value. We carried out cross-verification using another *ab initio* method, and the results are in reasonable agreement with the data presented above [see Table S1 of the Supplementary Information (SI)], confirming the exceptional charge transport properties of h-diamond. Since h-diamond has also been predicted to have a room-temperature thermal conductivity of nearly 2000 Wm⁻¹K⁻¹ [9, 11], it may outperform other novel semiconductors such as BAs, which has attracted considerable attention in recent years due to its high am-

* gaosp@fudan.edu.cn

† mchen@ast.com.cn

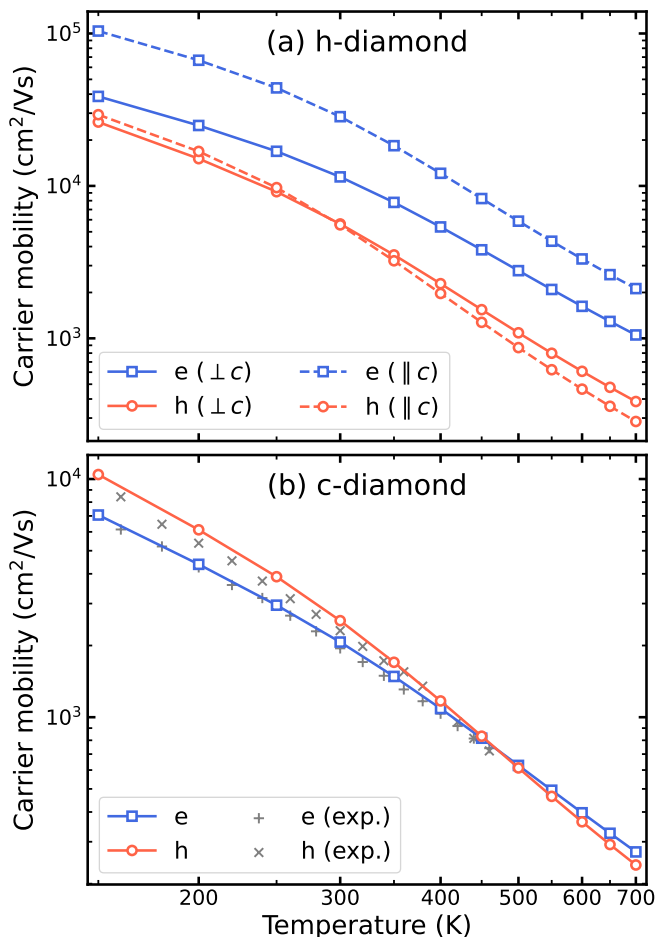


FIG. 1. Carrier mobilities of (a) h-diamond and (b) c-diamond, as functions of temperature. Experimental data are taken from Ref. 13.

bipolar mobility (about $1600 \text{ cm}^2\text{V}^{-1}\text{s}^{-1}$) [17, 18] and high thermal conductivity (about $1300 \text{ Wm}^{-1}\text{K}^{-1}$) [19–21]. Additionally, our G_0W_0 calculation yields a wide bandgap of 4.55 eV for h-diamond, and a molecular dynamics (MD) simulation at 1000 K indicates its thermal stability (see Fig. S1 of the SI). These combined properties suggest h-diamond as a promising candidate for applications in high-power and high-frequency electronics.

To pave the way for the high-temperature application of h-diamond, we examine the temperature dependence of its carrier mobility. Carrier mobility typically follows a power-law relationship with temperature, *i.e.*, $\mu \propto T^{-\alpha}$, if the scattering mechanism remains unchanged. However, as shown in Fig. 1(a), the temperature dependence of carrier mobility in h-diamond cannot be well described by a single power-law exponent α over the range of 150–700 K, suggesting a transition in the dominant scattering mechanism, which will be analysed in the subsequent section.

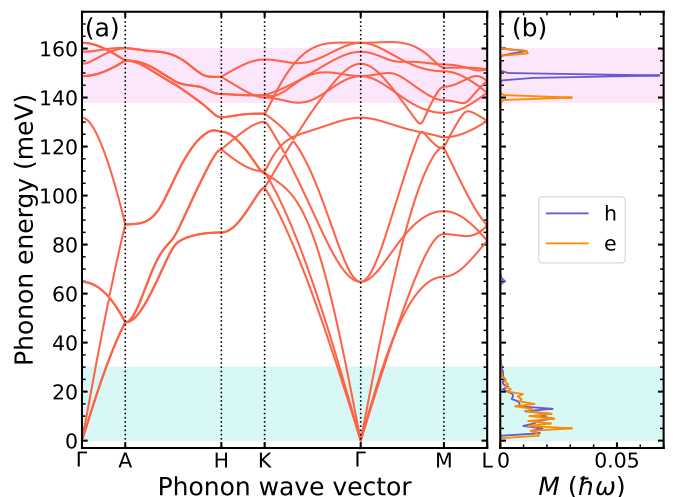


FIG. 2. (a) Phonon dispersion of h-diamond. (b) Calculated $M(\hbar\omega)$ at 300 K for holes and electrons. Two distinct frequency ranges indicating significant contributions to carrier scattering by acoustic phonons (marked in turquoise) and optical phonons (marked in violet) are highlighted. The vertical axes in (a) and (b) are aligned to enable direct comparison.

B. Carrier scattering mechanisms

Carrier mobility is governed by scattering mechanisms, an in-depth analysis of which can provide a better understanding of carrier transport behaviour at the microscopic level. In terms of electron-phonon (e-ph) interaction, since h-diamond is a non-polar semiconductor, deformation potential scattering is expected to play a central role, which can be induced by either acoustic or optical phonons. In order to elucidate the contributions of different phonon modes to carrier scattering, we define M as a function of phonon energy $\hbar\omega$ [Eq. (S6) in SI]. A larger value of $M(\hbar\omega)$ indicates a greater reduction in carrier mobility due to phonons with an energy around $\hbar\omega$. As shown in Fig. 2, carrier scattering is primarily induced by phonons in two energy ranges. The lower range is below 30 meV, attributed to acoustic deformation potential (ADP) scattering. The higher range is between 138 and 160 meV, corresponding to optical modes. At lower temperatures around 300 K, ADP is the predominant scattering mechanism. Nevertheless, as shown in Figs. S2 and S3 of the SI, the relative contribution of the optical deformation potential (ODP) scattering increases significantly at higher temperatures, dominating carrier-phonon scattering above about 400 K for holes and 450 K for electrons.

Both scattering mechanisms considerably depend on the carrier effective mass. A smaller effective mass typically indicates higher band velocities and a lower density of states (DOS), which give rise to faster carrier transport and reduced scattering phase space, respectively, thereby increasing mobility. For example, the high hole mobility in c-diamond is attributed primarily to its small effective

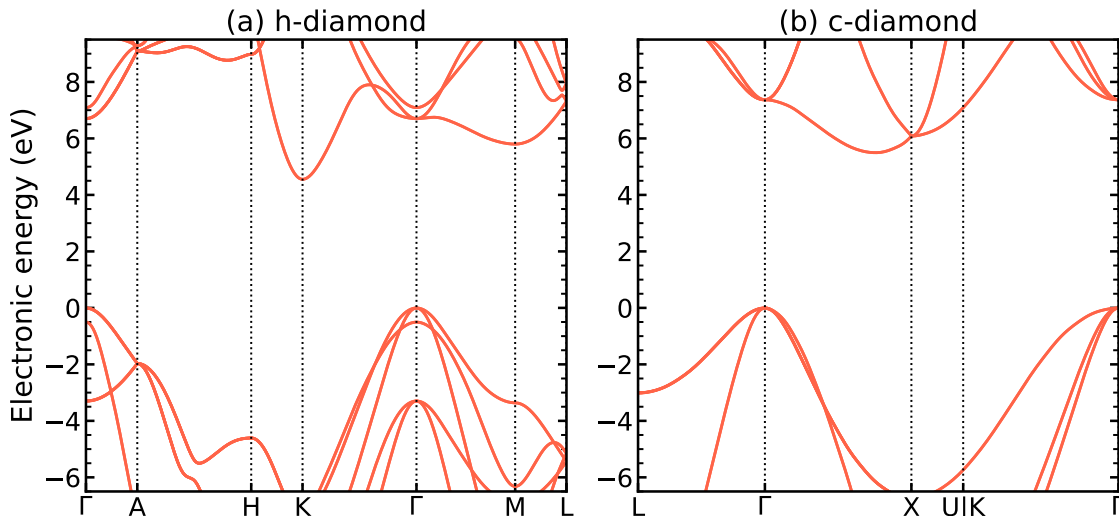


FIG. 3. G_0W_0 quasiparticle band structures of (a) h-diamond and (b) c-diamond. The fundamental gaps are (a) 4.55 eV and (b) 5.50 eV.

TABLE I. Calculated mobility effective masses, evaluated at 300 K and given in units of the electron rest mass. The definition is given in Eqs. (S8) and (S9) of the SI.

Carrier	h-diamond			c-diamond
	$\perp c$	$\parallel c$	average	
Hole	0.472	0.682	0.586	0.489
Electron	0.462	0.261	0.368	0.373

mass [22]. For comparison, we calculate the “mobility effective masses” [23] to quantify the effect of band curvature on carrier mobility, as listed in Table I. We also evaluate the DOS (per valley) near band edges, as shown in Fig. S4 of the SI. Both quantities of h-diamond are comparable to those of c-diamond, indicating that the small effective mass contributes considerably to the high mobility in h-diamond. However, it cannot further explain the fact that the mobility in h-diamond is significantly higher.

According to the relationship between the initial and final electronic states, carrier scattering can be divided into intraband and interband scattering, or intravalley and intervalley scattering. While intraband and intravalley scattering can always occur, the contributions of interband and intervalley scattering are primarily determined by the band structure. As shown in Fig. 3, the heavy-hole (hh) and light-hole (lh) bands (referred to as the highest and second highest valence bands, respectively) are close in energy, leading to interband scattering of holes. Regarding the conduction bands, the conduction band minimum (CBM) is away from the Brillouin zone centre, resulting in intervalley scattering between equivalent valleys.

For holes, the crystal-field splitting in h-diamond opens an appreciable energy gap between the valence

band maximum (VBM) and the split-off hole (sh) band, whereas in c-diamond, this gap is only 16 meV at the Γ point. It is thus natural to consider whether the lower hole mobility in c-diamond arises from the additional interband scattering channels that involve the sh band. However, the DOS near the VBM is actually comparable in both phases, as shown in Fig. S4 of the SI. To provide a quantitative analysis, we computed the room-temperature hole mobility with the sh band artificially excluded from the calculation. The result shows a slight increase in hole mobility of approximately 2%.

Regarding electrons, the CBM of c-diamond lies at the Δ point and has a larger multiplicity than the CBM of h-diamond (located at K). To compare the relative contributions of intervalley scattering in both materials, we calculated the room-temperature electron mobility that only involves the scattering induced by phonons with wave vector lengths below a specific cutoff, *i.e.*, $|\mathbf{q}|_{\text{cut}}$. Since intravalley scattering is mediated by phonons with small $|\mathbf{q}|$, and the CBM valleys are well separated from their equivalent counterparts in both phases, the mobility- $|\mathbf{q}|_{\text{cut}}$ relationship directly decomposes the contributions of intervalley and intravalley scattering. As shown in Fig. S5 of the SI, intravalley scattering significantly dominates in h-diamond. In c-diamond, despite the multiple intervalley scattering paths (including g -processes and f -processes), the g -processes play a negligible role, and the overall contribution of intervalley scattering is comparable to that in h-diamond, which is approximately 10%.

Therefore, the mobility difference between the two phases cannot be explained by either the interband scattering that involves the sh band or the intervalley scattering of electrons, suggesting that other factors should play a crucial role. According to the results above, we will henceforth focus on intravalley scattering and restrict our analysis to the hh and lh bands.

C. Origin of the higher hole mobility in h-diamond

For holes in *c*-diamond, the room-temperature mobility is predominantly limited by transverse acoustic (TA) phonons (see Fig. S6 of the SI), which agrees with the previous study [22], and longitudinal acoustic (LA) phonons also play an appreciable role. These observations can be understood according to the selection rules (the notation for irreducible representations follows that of Ref. 24; see also Fig. S7 of the SI).

$$\begin{aligned} \langle 100 \rangle : \\ \Gamma'_{25} \otimes \Delta'_2 &= \Delta_1 \oplus \Delta_5 = \text{TA} + \text{LA} + \text{TO} \\ \Gamma'_{25} \otimes \Delta_5 &= \Delta_1 \oplus \Delta'_1 \oplus \Delta_2 \oplus \Delta'_2 \oplus \Delta_5 \\ &= \text{TA} + \text{LA} + \text{TO} + \text{LO} \end{aligned} \quad (1)$$

$$\begin{aligned} \langle 110 \rangle : \\ \Gamma'_{25} \otimes \Sigma_2 &= \Sigma_1 \oplus \Sigma_2 \oplus \Sigma_4 = \text{TA}_1 + \text{LA} + \text{TO} \\ \Gamma'_{25} \otimes \Sigma_1 &= \Sigma_1 \oplus \Sigma_2 \oplus \Sigma_3 = \text{TA}_2 + \text{LA} + \text{TO} + \text{LO} \end{aligned} \quad (2)$$

$$\begin{aligned} \langle 111 \rangle : \\ \Gamma'_{25} \otimes \Lambda_3 &= \Lambda_1 \oplus \Lambda_2 \oplus 2\Lambda_3 = \text{TA} + \text{LA} + \text{TO} + \text{LO} \end{aligned} \quad (3)$$

Therefore, the symmetry imposes little restriction on acoustic modes. The scattering processes mediated by LA phonons are allowed for all these directions, and those induced by TA modes are only partially forbidden.

For h-diamond, the VBM is composed of p_x and p_y orbitals and has Γ_5^+ symmetry. The selection rules for in-plane scattering are

$$\Gamma_5^+ \otimes \Sigma_2 = \Sigma_1 \oplus \Sigma_3, \quad \Gamma_5^+ \otimes \Sigma_4 = \Sigma_1 \oplus \Sigma_3, \quad (4)$$

which originate from the symmetry of the Lonsdaleite structure. Since both the initial and final states are odd under (0001) mirror symmetry, phonons that are odd under it, such as the out-of-plane TA mode, are forbidden from inducing such transitions, thereby reducing the number of available scattering channels. By contrast, although both h-diamond and wurtzite structures exhibit the AB stacking and share hexagonal symmetry, the compound nature of the latter breaks the (0001) mirror symmetry. Consequently, all phonon modes are allowed by symmetry to induce in-plane scattering in wurtzite structures. The selection rule for scattering with $\mathbf{q} \parallel c$ is

$$\Gamma_5^+ \otimes \Delta_5 = \Delta_1 \oplus \Delta_2 \oplus \Delta_6, \quad (5)$$

indicating that both TA modes (Δ_5 symmetry) are forbidden. In conjunction with Eq. (4), the selection rules considerably suppress TA-scattering in h-diamond, which predominantly limits hole mobility in *c*-diamond around room temperature. This suppression significantly contributes to the higher hole mobility in h-diamond.

Meanwhile, h-diamond contains four atoms in its primitive cell, giving rise to six additional phonon modes compared with *c*-diamond. To elucidate the effect of these extra modes on hole mobility, we first focus on the “high-energy” optical phonons with $\hbar\omega \geq 132$ meV. In *c*-diamond, transverse optical (TO) modes are allowed by selection rules [Eqs. (1)–(3)] to induce hole scattering, while scattering mediated by longitudinal optical (LO) phonons is forbidden for final states at the hh band along $\langle 100 \rangle$ and $\langle 110 \rangle$ directions. This also explains the trend observed in Fig. S6 of the SI that TO phonons become dominant at elevated temperatures, whereas LO phonons have a limited effect even at 700 K. In h-diamond, there are six optical branches within this range. Nevertheless, for both $\perp c$ and $\parallel c$ directions, only two TO modes (Δ_6 and Σ_1 symmetry) and one LO mode (Δ_1 and Σ_3 symmetry) are allowed by selection rules [Eqs. (4) and (5)] to mediate hole scattering. Hence, the high-energy optical phonons introduce few additional scattering channels in h-diamond. However, LO-induced scattering is less restricted by selection rules compared with *c*-diamond, which could account for the trend in Fig. 1 that the relative difference in hole mobility between the two phases becomes smaller at higher temperatures.

The “low-energy” ($\hbar\omega < 132$ meV) optical phonons in h-diamond along high-symmetry paths consist of two interlayer shear modes and one interlayer breathing mode. For in-plane scattering, the shear modes are forbidden due to their odd parity under reflection across the (0001) plane. For hole scattering along the *c*-axis, the breathing mode (Δ_3 symmetry) is also forbidden [Eq. (5)]. In contrast, the breathing mode with $\mathbf{q} \perp c$ and the shear modes with $\mathbf{q} \parallel c$ are allowed to mediate scattering, leading to non-zero matrix elements. These modes are characterised by shear or stretching vibrations of bonds parallel to the *c*-axis. As shown in Fig. 4, the VBM exhibits an in-plane charge density distribution due to its p_x - p_y character. Therefore, the spatial separation between the in-plane charge distribution and the scattering potentials leads to weak carrier-phonon coupling in this regime.

On the other hand, the in-plane charge density distribution at the VBM also leads to anisotropy in the hole effective mass, which is larger parallel to the *c*-axis (Table I). This is consistent with the hole mobility based on the self-energy relaxation time approximation (SERTA), which is 23% lower along *z* than in the *xy* directions at 300 K. Nonetheless, the Boltzmann transport equation (BTE) reveals a different trend: at 300 K, the mobility is almost identical along three Cartesian directions; at lower temperatures, the *z*-component is even higher than the *xy*-components. This enhancement of hole mobility along *z* can be attributed to weak scattering by phonons with $\mathbf{q} \parallel c$. According to Eq. (5), both TA modes are forbidden from inducing out-of-plane scattering. Although LA phonons are allowed to mediate scattering, they correspond to displacements of basal planes along the *c*-axis, resulting in suppressed interactions with the in-plane charge distribution, similar to the case of

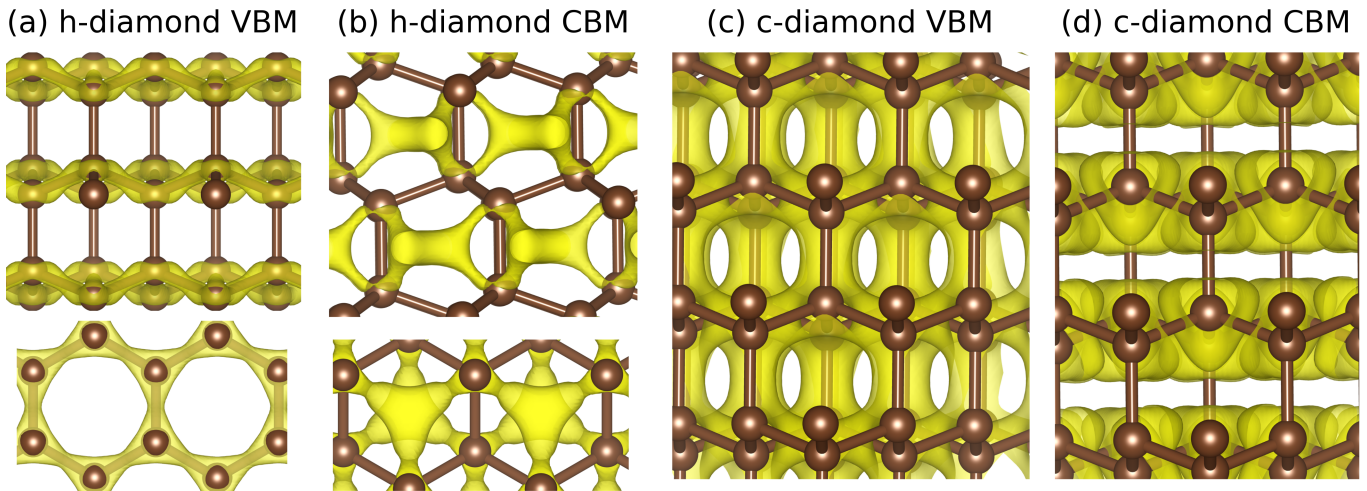


FIG. 4. Real-space distributions of charge density at VBM or CBM. The isosurfaces denote the values of (a) 3.5×10^{-4} , (b) 1.8×10^{-3} , (c) 7×10^{-4} , and (d) 1.08×10^{-3} a.u., respectively. Visualised using VESTA [25].

interlayer shear and breathing modes discussed in the previous paragraph. In contrast, for $\mathbf{q} \perp c$, scattering by the LA and in-plane TA modes is allowed, both of which involve intralayer vibrations, leading to considerable carrier-phonon coupling. Hence, the z -component of hole band velocity is subject to little change due to scattering, enhancing mobility along this direction. This also explains the underestimation of SERTA, which assumes a complete loss of carrier momentum after each scattering event and is likely to overestimate anisotropic scattering. At higher temperatures, high-energy optical modes exhibiting in-plane opposite vibrations are activated. As a result, phonons with $\mathbf{q} \parallel c$ can now induce significant scattering. Consequently, the hole mobility along the z direction becomes lower than the xy -components above 300 K. At 700 K, the z -component of BTE mobility is only 6% higher than its SERTA counterpart.

D. Origin of the higher electron mobility in h-diamond

For electron scattering, the selection rules along the three Cartesian directions are evaluated. In *c*-diamond, the constant-energy surfaces near the CBM [located at the Δ point with a Cartesian coordinate of $(u, 0, 0)$] are ellipsoids. The selection rule for intravalley scattering along the principal axis is

$$\Delta_1 \otimes \Delta_1 = \Delta_1 = \text{LA}, \quad (6)$$

while that for scattering perpendicular to the principal axis is

$$\Delta_1 \otimes A_1 = \Delta_1 \oplus \Delta_2 \oplus \Delta_5 = \text{TA} + \text{LA} + \text{TO}, \quad (7)$$

where the A point has a Cartesian coordinate of $(u, v, 0)$. In h-diamond (CBM at K), the selection rules are

$$x\text{-direction} : K_2^+ \otimes \Lambda_3 = \Lambda_1, \quad (8)$$

$$y\text{-direction} : K_2^+ \otimes B_1 = \Sigma_1 \oplus \Sigma_3, \quad (9)$$

$$z\text{-direction} : K_2^+ \otimes P_2 = \Delta_1 \oplus \Delta_4. \quad (10)$$

In both phases, LA phonons (of Λ_1 , Δ_1 , and Σ_1 symmetry in h-diamond) are allowed to induce scattering, whereas transitions mediated by TA modes (of Σ_3 , Σ_4 , Λ_3 , Λ_4 , and Δ_5 symmetry in h-diamond) are forbidden in specific directions. Compared with *c*-diamond, TA phonons in h-diamond are subject to stricter restrictions, which reduce the number of scattering channels, similar to the case of hole transport. Consequently, the TA modes contribute about 2/3 of the total scattering in *c*-diamond at 300 K, whereas such a contribution is below 30% in h-diamond. Nevertheless, optical phonons have a more significant influence in h-diamond than in *c*-diamond, partially offsetting the effect of suppressed TA-scattering. Therefore, the difference in selection rules may be insufficient to account for the substantially higher electron mobility in h-diamond.

Instead, the charge distribution provides a possible explanation. As shown in Fig. 4(b), the CBM state in h-diamond is composed of antibonding p_x - p_y orbitals, consistent with the D_{3h} point-group symmetry at the K points. The corresponding charge density is delocalised over the interstitial regions of the lattice, contributing to a small effective mass. Moreover, since h-diamond is non-polar and thus lacks the long-range Fröhlich interaction, scattering potentials are concentrated near atoms and bonds, leading to weak spatial overlap with the CBM wavefunction, as visualised in Fig. 5. Such a “decoupling” between electrons and phonons considerably decreases the values of matrix elements (Fig. S8 of the SI), thereby reducing the scattering rate and playing a crucial role in the exceptionally high electron mobility of h-diamond.

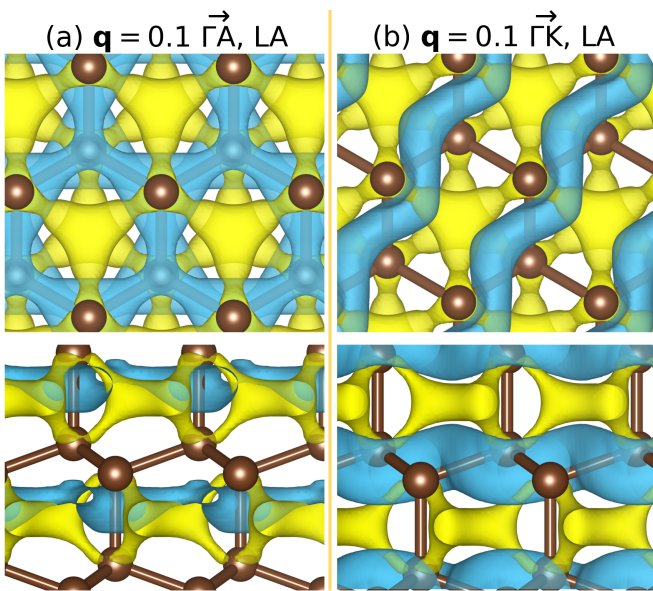


FIG. 5. Real-space distribution of the CBM charge density (yellow) and the phonon-induced scattering potential (blue) for two representative LA phonons in h-diamond. Top and bottom rows show views along $\langle 0001 \rangle$ and $\langle 1000 \rangle$ directions, respectively. The isosurface levels are set to 1.8×10^{-4} a.u. for the charge density, and to 0.01 and 0.0915 a.u. for the scattering potentials in (a) and (b), respectively.

III. DISCUSSION

In summary, we reveal the exceptionally high mobility in h-diamond and elucidate its physical origins. ADP scattering mediated by TA phonons, which is the predominant scattering mechanism for holes in c-diamond around room temperature, is considerably suppressed in h-diamond by selection rules. The in-plane distribution of the VBM wavefunction also leads to weak interactions with the additional interlayer shear and breathing modes in h-diamond. For electrons, the CBM wavefunction formed by antibonding p_x - p_y orbitals is distributed primarily in the interstitial regions within the h-diamond lattice, giving rise to little overlap with scattering potentials, thus significantly enhancing electron mobility. Other factors including effective mass are comparable in the two phases, contributing negligibly to their mobility difference. We also show the temperature dependence of carrier mobility, which deviates from the power-law relationship due to the increased occupation of high-energy optical phonons at elevated temperatures. Our findings indicate h-diamond as a promising candidate for high-frequency and high-speed applications. Furthermore, by revealing the significance of selection rules and electron-phonon “decoupling”, this work offers fresh insights into the mechanisms associated with high carrier mobility.

IV. METHODS

A. DFT and DFPT calculations

Geometry optimisation and phonon calculations were performed using the QUANTUM ESPRESSO software [26–28]. The Broyden-Fletcher-Goldfarb-Shanno (BFGS) algorithm was utilised for geometry optimisation, with the convergence thresholds for energy, force, and stress set to 10^{-9} Ry, 10^{-6} Ry/Bohr, and 0.05 kbar, respectively. Phonon calculations were based on density-functional perturbation theory (DFPT), with a convergence threshold of 10^{-17} . Optimised norm-conserving Vanderbilt pseudopotentials [29] with full relativistic treatment from the PSEUDO DOJO project [30] were used, and the plane-wave cutoff energy was chosen to be 100 Ry. The PBEsol functional [31] was applied for the approximation of exchange-correlation interaction.

B. GW band structure calculations

In order to obtain accurate ε - \mathbf{k} dispersion relationships, quasi-particle eigenvalues were calculated using the one-shot G_0W_0 method, as implemented in the YAMBO software [32, 33]. The band structures and DOS were then obtained based on the maximally localised Wannier functions (MLWFs) [34, 35] as implemented in the WANNIER90 code [36].

C. e-ph scattering and mobility calculations

For the calculations of e-ph scattering and carrier mobility, the electronic Hamiltonians, dynamical matrices, and electron-phonon matrix elements were interpolated onto ultrafine \mathbf{k} and \mathbf{q} grids based on MLWFs using the EPW code [37, 38]. The energy window was set to 0.3 eV (relative to the band edge), and the grid sizes are listed in Table S2 of the SI. The spin-orbit coupling (SOC) was found to have a negligible effect on electron mobility and was thus only considered for valence bands. To ensure the accurate description of long-range interactions, the effect of dynamical quadrupoles was included, which were calculated based on DFPT using the ABINIT software [39, 40].

For cross-verification, carrier mobilities were also calculated using the ABINIT software [39, 40]. The electronic states were obtained directly from non-self-consistent calculations, and Fourier interpolations were used for the scattering potentials.

D. MD simulation

In order to examine the thermal stability of h-diamond, we performed a MD simulation in the NPT ensemble at

1000 K and 1 atm. The time step was chosen to be 1 fs, and the MD simulation ran for 10,000 steps (*i.e.*, 10 ps). Forces and pressures were calculated based on DFT using the Gaussian and plane wave (GPW) method as implemented in the CP2K code [41], employing the DZVP-MOLOPT basis set. The cutoff energy and the relative cutoff energy were set to 300 and 50 Ry, respectively. The exchange-correlation interaction was approximated by the PBEsol functional [31]. A $8 \times 8 \times 5$ supercell containing 1280 atoms was used, and the BZ was sampled with a single Γ -point.

DATA AVAILABILITY

The data that support the findings of this work are available from the corresponding authors upon reasonable requests.

CODE AVAILABILITY

All computational codes used in this work (QUANTUM ESPRESSO, EPW, ABINIT, YAMBO, WANNIER90, and

CP2K) are open-source and available online.

COMPETING INTERESTS

The authors declare no competing interests.

AUTHOR CONTRIBUTIONS

Z. H., S. G., and M. C. conceptualised and designed this study. Z. H. performed the calculations, analysed the results, and wrote the initial draft. S. G. and M. C. edited the manuscript and supervised the project. All authors reviewed and approved the final version of the manuscript.

ACKNOWLEDGMENTS

This work was supported by research funds from Shanghai Advanced Silicon Technology Co., Ltd., and also the Natural Science Foundation of Shanghai (Grant No. 23ZR1403300).

-
- [1] C. J. Wort and R. S. Balmer, Diamond as an electronic material, *Mater. Today* **11**, 22 (2008).
- [2] J. S. Blakemore, Semiconducting and other major properties of gallium arsenide, *J. Appl. Phys.* **53**, R123 (1982).
- [3] Z. Galazka, β -Ga₂O₃ for wide-bandgap electronics and optoelectronics, *Semicond. Sci. Technol.* **33**, 113001 (2018).
- [4] S. Shikata, Single crystal diamond wafers for high power electronics, *Diam. Relat. Mater.* **65**, 168 (2016).
- [5] C. Frondel and U. Marvin, Lonsdaleite, a hexagonal polymorph of diamond, *Nature (London)* **214**, 587 (1967).
- [6] R. E. Hanneman, H. M. Strong, and F. P. Bundy, Hexagonal diamonds in meteorites: Implications, *Science* **155**, 995 (1967).
- [7] F. P. Bundy and J. S. Kasper, Hexagonal diamond—a new form of carbon, *J. Chem. Phys.* **46**, 3437 (1967).
- [8] Z. Pan, H. Sun, Y. Zhang, and C. Chen, Harder than diamond: Superior indentation strength of wurtzite BN and lonsdaleite, *Phys. Rev. Lett.* **102**, 055503 (2009).
- [9] J. Zhang, Z. Zhao, M. Jiang, Y. Cheng, and G. Zhang, Thermal properties of hexagonal diamond: Machine learning potential and molecular dynamics study, *Phys. Rev. Mater.* **9**, 094603 (2025).
- [10] L. Shi, X. Ma, Y. Zhong, M. Li, W. Yin, L. Yang, and X. He, Phonon thermal transport in diamond and lonsdaleite: A comparative study of empirical potentials, *Diam. Relat. Mater.* **120**, 108618 (2021).
- [11] P. Chakraborty, G. Xiong, L. Cao, and Y. Wang, Lattice thermal transport in superhard hexagonal diamond and wurtzite boron nitride: A comparative study with cubic diamond and cubic boron nitride, *Carbon* **139**, 85 (2018).
- [12] L. Yang, K. C. Lau, Z. Zeng, D. Zhang, H. Tang, B. Yan, G. Niu, H. Gou, Y. Yang, W. Yang, *et al.*, Synthesis of bulk hexagonal diamond, *Nature (London)* **644**, 370 (2025).
- [13] M. Gabrysch, S. Majdi, D. J. Twitchen, and J. Isberg, Electron and hole drift velocity in chemical vapor deposition diamond, *J. Appl. Phys.* **109**, 063719 (2011).
- [14] F. J. Morin, Lattice-scattering mobility in germanium, *Phys. Rev.* **93**, 62 (1954).
- [15] H. Hicks and D. Manley, High purity GaAs by liquid phase epitaxy, *Solid State Commun.* **7**, 1463 (1969).
- [16] Y. Zheng, S. Lu, C. Chen, M. Jiang, X. Li, and X. Hu, Pure hexagonal diamond with symmetry-doping properties, *ACS Appl. Mater. Interfaces* **16**, 52674 (2024).
- [17] S. Yue, F. Tian, X. Sui, M. Mohebinia, X. Wu, T. Tong, Z. Wang, B. Wu, Q. Zhang, Z. Ren, J. Bao, and X. Liu, High ambipolar mobility in cubic boron arsenide revealed by transient reflectivity microscopy, *Science* **377**, 433 (2022).
- [18] J. Shin, G. A. Gamage, Z. Ding, K. Chen, F. Tian, X. Qian, J. Zhou, H. Lee, J. Zhou, L. Shi, T. Nguyen, F. Han, M. Li, D. Broido, A. Schmidt, Z. Ren, and G. Chen, High ambipolar mobility in cubic boron arsenide, *Science* **377**, 437 (2022).
- [19] J. S. Kang, M. Li, H. Wu, H. Nguyen, and Y. Hu, Experimental observation of high thermal conductivity in boron arsenide, *Science* **361**, 575 (2018).
- [20] S. Li, Q. Zheng, Y. Lv, X. Liu, X. Wang, P. Y. Huang, D. G. Cahill, and B. Lv, High thermal conductivity in cubic boron arsenide crystals, *Science* **361**, 579 (2018).
- [21] F. Tian *et al.*, Unusual high thermal conductivity in boron arsenide bulk crystals, *Science* **361**, 582 (2018).
- [22] Q.-L. Yang, F.-C. Meng, W. Li, Z. Wang, H.-X. Deng, S.-H. Wei, F.-I. Ning, and J.-W. Luo, First-principles investigation of microscopic mechanisms underlying hole mo-

- bilities in diamond, silicon, and germanium, *Phys. Rev. B* **110**, 155203 (2024).
- [23] S. Ponc e, F. Macheda, E. R. Margine, N. Marzari, N. Bonini, and F. Giustino, First-principles predictions of Hall and drift mobilities in semiconductors, *Phys. Rev. Res.* **3**, 043022 (2021).
- [24] M. S. Dresselhaus, G. Dresselhaus, and A. Jorio, *Group Theory: Application to the Physics of Condensed Matter* (Springer Berlin, Heidelberg, 2008).
- [25] K. Momma and F. Izumi, *VESTA3* for three-dimensional visualization of crystal, volumetric and morphology data, *Journal of Applied Crystallography* **44**, 1272 (2011).
- [26] P. Giannozzi *et al.*, QUANTUM ESPRESSO: a modular and open-source software project for quantum simulations of materials, *J. Phys.: Condens. Matter* **21**, 395502 (2009).
- [27] P. Giannozzi *et al.*, Advanced capabilities for materials modelling with Quantum ESPRESSO, *J. Phys.: Condens. Matter* **29**, 465901 (2017).
- [28] P. Giannozzi, O. Baseggio, P. Bonf a, D. Brunato, R. Car, I. Carnimeo, C. Cavazzoni, S. de Gironcoli, P. Delugas, F. Ferrari Ruffino, A. Ferretti, N. Marzari, I. Timrov, A. Urru, and S. Baroni, Quantum ESPRESSO toward the exascale, *J. Chem. Phys.* **152**, 154105 (2020).
- [29] D. R. Hamann, Optimized norm-conserving Vanderbilt pseudopotentials, *Phys. Rev. B* **88**, 085117 (2013).
- [30] M. van Setten, M. Giantomassi, E. Bousquet, M. Verstraete, D. Hamann, X. Gonze, and G.-M. Rignanese, The PseudoDojo: Training and grading a 85 element optimized norm-conserving pseudopotential table, *Comput. Phys. Commun.* **226**, 39 (2018).
- [31] J. P. Perdew, A. Ruzsinszky, G. I. Csonka, O. A. Vydrov, G. E. Scuseria, L. A. Constantin, X. Zhou, and K. Burke, Restoring the density-gradient expansion for exchange in solids and surfaces, *Phys. Rev. Lett.* **100**, 136406 (2008).
- [32] A. Marini, C. Hogan, M. Gruening, and D. Varsano, yambo: An *ab initio* tool for excited state calculations, *Comp. Phys. Commun.* **180**, 1392 (2009).
- [33] D. Sangalli, A. Ferretti, H. Miranda, C. Attaccalite, I. Marri, E. Cannuccia, P. Melo, M. Marsili, F. Paleari, A. Marrazzo, G. Prandini, P. Bonf a, M. O. Atambo, F. Affinito, M. Palumbo, A. Molina-S anchez, C. Hogan, M. Gr uning, D. Varsano, and A. Marini, Many-body perturbation theory calculations using the yambo code, *J. Phys.: Condens. Mat.* **31**, 325902 (2019).
- [34] N. Marzari and D. Vanderbilt, Maximally localized generalized Wannier functions for composite energy bands, *Phys. Rev. B* **56**, 12847 (1997).
- [35] I. Souza, N. Marzari, and D. Vanderbilt, Maximally localized Wannier functions for entangled energy bands, *Phys. Rev. B* **65**, 035109 (2001).
- [36] G. Pizzi *et al.*, Wannier90 as a community code: new features and applications, *J. Phys.: Condens. Matter* **32**, 165902 (2020).
- [37] S. Ponc e, E. Margine, C. Verdi, and F. Giustino, EPW: Electron-phonon coupling, transport and superconducting properties using maximally localized Wannier functions, *Comput. Phys. Commun.* **209**, 116 (2016).
- [38] H. Lee, S. Ponc e, K. Bushick, S. Hajinazar, J. Lafuente-Bartolome, J. Leveillee, C. Lian, J. Lihm, F. Macheda, H. Mori, H. Paudyal, W. Sio, S. Tiwari, M. Zacharias, X. Zhang, N. N. Bonini, E. Kioupakis, E. Margine, and F. Giustino, Electron-phonon physics from first principles using the EPW code, *npj Comput. Mater.* **9**, 156 (2023).
- [39] X. Gonze *et al.*, The abinit project: Impact, environment and recent developments, *Comput. Phys. Commun.* **248**, 107042 (2020).
- [40] A. H. Romero *et al.*, ABINIT: Overview, and focus on selected capabilities, *J. Chem. Phys.* **152**, 124102 (2020).
- [41] T. D. K uhne *et al.*, CP2K: An electronic structure and molecular dynamics software package - quickstep: Efficient and accurate electronic structure calculations, *J. Chem. Phys.* **152**, 194103 (2020).